

Feedback-based Quantum Algorithm Inspired by Counterdiabatic Driving

Rajesh K. Malla,^{1,*} Hiroki Sukeno,² Hongye Yu,² Tzu-Chieh Wei,² Andreas Weichselbaum,¹ and Robert M. Konik¹

¹*Condensed Matter Physics and Materials Science Division,
Brookhaven National Laboratory, Upton, New York 11973, USA*

²*C.N. Yang Institute for Theoretical Physics & Department of Physics and Astronomy,
Stony Brook University, Stony Brook, New York 11794, USA*

(Dated: July 25, 2024)

In recent quantum algorithmic developments, a feedback-based approach has shown promise for preparing quantum many-body system ground states and solving combinatorial optimization problems. This method utilizes quantum Lyapunov control to iteratively construct quantum circuits. Here, we propose a substantial enhancement by implementing a protocol that uses ideas from quantum Lyapunov control and the counterdiabatic driving protocol, a key concept from quantum adiabaticity. Our approach introduces an additional control field inspired by counterdiabatic driving. We apply our algorithm to prepare ground states in one-dimensional quantum Ising spin chains. Comprehensive simulations demonstrate a remarkable acceleration in population transfer to low-energy states within a significantly reduced time frame compared to conventional feedback-based quantum algorithms. This acceleration translates to a reduced quantum circuit depth, a critical metric for potential quantum computer implementation. We validate our algorithm on the IBM cloud computer, highlighting its efficacy in expediting quantum computations for many-body systems and combinatorial optimization problems.

I. INTRODUCTION

The quest for efficient quantum algorithms for many-body ground state preparation has been a central focus in quantum simulation research [1–5], marked by the evolution from early adiabatic approaches to recent quantum-classical hybrid structures. Early approaches leveraged the concept of adiabaticity utilizing an effective time-dependent Hamiltonian to undergo a gradual time evolution from an initial state to the ground state at large times. These types of algorithms can be categorized by either quantum adiabatic algorithm [6–9] or quantum annealing [10–12]. In contrast, recent advancements in quantum algorithms have shifted towards quantum-classical hybrid structures, harnessing the combined effect of both quantum and classical computing. This approach is particularly apt for the era of noisy intermediate-scale quantum (NISQ) devices [13]. These algorithms are known as variational quantum algorithms (VQA) [14–19], with some notable examples including the Quantum Approximate Optimization Algorithm (QAOA) [20–22] and the Variational Quantum Eigensolver (VQE) [23–26]. These algorithms have demonstrated superior performance compared to classical counterparts, particularly in addressing combinatorial problems [27, 28] and challenges in quantum chemistry [23, 29]. We note, however, that classical optimization within variational quantum algorithms often faces numerical challenges due to optimization landscapes that contain false local minima and barren plateaus [30–35].

Recently, a novel quantum algorithm named the Feedback-Based Quantum Algorithm (FQA) has been introduced [36, 37]. This approach draws inspiration from

the principles of Quantum Lyapunov Control (QLC) [38, 39], negating the necessity for predetermined time evolution or classical optimization. Instead, FQA constructs the quantum circuit iteratively, introducing new layers where the parameters are meticulously determined through feedback derived from qubit measurements in the preceding layer. A fundamental unit, called a layer, in the FQA architecture comprises two unitaries, echoing the structure found in QAOA and quantum annealing. These unitaries represent the parent Hamiltonian governing the desired ground state and a mixer Hamiltonian, the ground state of which serves as the algorithm's initial state. This innovative methodology represents a departure from conventional approaches, exemplifying the potential of QLC in shaping the landscape of quantum algorithms.

This work presents a significant enhancement to the FQA through the integration of the counterdiabatic driving protocol [40], formally termed the Counterdiabatic Feedback-Based Quantum Algorithm (CD-FQA). While FQA draws upon QLC principles, counterdiabaticity, a concept derived from adiabaticity, is employed to effect rapid changes in the time-dependent Hamiltonian without inducing nonadiabatic transitions. The utilization of counterdiabaticity in quantum circuits has been previously applied within the framework of VQA [41–43]. Here, we explore the dynamic interplay between QLC and counterdiabaticity, applying these principles to the design of quantum circuits for the ground-state preparation of Hamiltonians representing one-dimensional (1D) Ising model Hamiltonians. Distinct from FQA, each layer in CD-FQA includes a third unitary inspired by the counterdiabatic driving protocol, see Fig. 1. This addition results in a notable reduction in depth compared to the standard FQA. The selection of the third unitary is performed from a pool of counterdiabatic operators. It is

* rmalla@bnl.gov

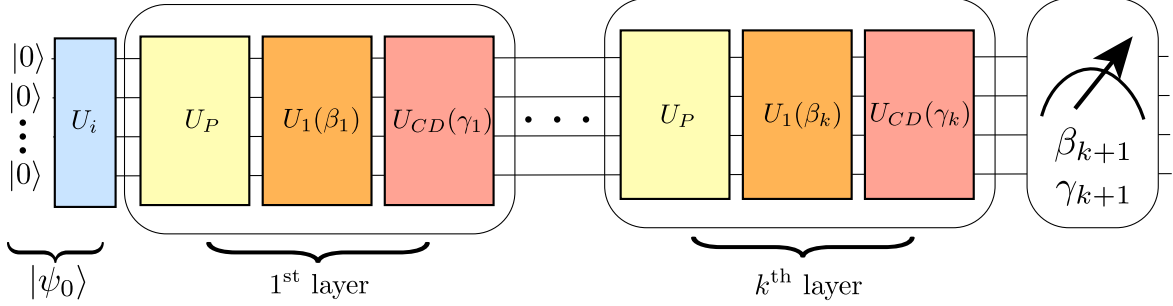


FIG. 1. The schematic diagram of the CD-FQA quantum circuit up to k^{th} layer is shown. The $(k + 1)^{\text{th}}$ layer is parameterized by β_{k+1} and γ_{k+1} . These are obtained by measuring the respective commutator expectation values $\beta_{k+1} = i\langle\psi_k|[H_P, H_1]\rangle\psi_k$ and $\gamma_{k+1} = i\langle\psi_k|[H_P, H_{CD}]\rangle\psi_k$.

demonstrated that an improper choice from this pool can lead to convergence issues in the dynamics. The implications of these findings are discussed in the context of advancing quantum algorithms for ground-state preparation.

The article is structured as follows: Sec. II provides a review of QLC, while Sec. III establishes a connection between the counterdiabatic driving protocol and QLC, exploring the selection of the second control Hamiltonian for the CD-FQA. In Sec. IV we present the CD-FQA, comparing complexities with the standard FQA. Section V applies the CD-FQA to diverse Ising models and discusses the outcomes. Section VI demonstrates the implementation of CD-FQA on cloud quantum computers. Section VII discusses various implications of CD-FQA, and the conclusion is presented in Sec. VIII.

II. QUANTUM LYAPUNOV CONTROL

Quantum Lyapunov Control (QLC) represents a form of quantum control engineered to guide a quantum system from an arbitrary initial state, denoted as $|\psi_i\rangle$, to a specified final state, $|\psi_f\rangle$. This steering process is facilitated by a target-specific control function $V(t)$, referred to as the Lyapunov function. The design of such controlled dynamics often involves placing constraints on the Lyapunov function.

Consider, for instance, the task of preparing the ground state of a many-body system for a given physical or *problem* Hamiltonian H_P . In cases where the ground state is initially unknown, the system's energy $E_P(t) = \langle\psi(t)|H_P|\psi(t)\rangle \equiv \langle H_P \rangle_t$ naturally emerges as a suitable Lyapunov function. The controlled dynamics is formulated to adhere to the constraint $\frac{d}{dt}E_P \equiv \dot{E}_P \leq 0$, ensuring that at each time step, the system's energy experiences a decrement. This condition guarantees a systematic reduction in the system's energy as the controlled evolution unfolds.

Let us begin with a driven quantum system, where the dynamics is governed by the Schrödinger equation

$$i\frac{d}{dt}|\psi(t)\rangle = (H_P + H_C(t))|\psi(t)\rangle, \quad (1)$$

where H_P is the problem Hamiltonian as above, and $H_C(t)$ is the *control Hamiltonian*. For convenience, we set $\hbar = 1$, throughout. The control Hamiltonian $H_C(t)$ can be expressed in the general form

$$H_C(t) = \sum_{m=1}^M \beta_m(t) H_m. \quad (2)$$

In this formulation, the H_m 's represent $m = 1, \dots, M$ time-independent Hermitian *mixing* operators, with the time-dependence embedded in the real-valued control fields $\beta_m(t)$. These control parameters are chosen such that they ensure a negative rate of change of the energy $E_P(t) \equiv \langle H_P \rangle_t$ of the problem Hamiltonian,

$$\begin{aligned} \frac{d}{dt}E_P(t) &= i\langle[H_C, H_P]\rangle_t \\ &= \sum_m \beta_m(t) \underbrace{i\langle[H_m, H_P]\rangle_t}_{\equiv A_m(t)} \equiv \beta(t) \cdot \mathbf{A}(t) \leq 0, \end{aligned} \quad (3)$$

with real-valued M -dimensional vectors β and \mathbf{A} in the last expression, and expectation values are obtained with respect to the wavefunction $\psi(t)$. To ensure negative $\dot{E}_P(t) \leq 0$, the conventional choice for the control field is used $\beta(t) = -\alpha \mathbf{A}(t)$ with $\alpha > 0$. We note that when the system size, N , increases the expectation value of commutators $A_m(t)$ increases linearly with system size. Therefore, to keep the protocol system independent, we choose

$$\beta(t) = -\alpha \frac{1}{N J^2} \mathbf{A}(t), \quad (4)$$

where we applied a factor $1/J^2$ on the r.h.s. to make both, α and β dimensionless, and J is the energy scale of the system. Then, each protocol can be defined by a fixed α that is independent of the system size.

While usually $M = 1$, the QLC method seamlessly extends to scenarios involving multiple control fields, $M > 1$. The inclusion of additional parameters therefore emerges as an intuitive approach to expedite the preparation of the target state. The Lyapunov function, derived from the solution of Eq. (1), converges to the minimum of $E_P(t)$ under specific sufficient conditions [38, 39, 44, 45].

Furthermore, the state converges to a set of states characterized by La Salle's invariance principle [46].

In the subsequent section, we demonstrate that these additional control fields can be derived from a pool of operators commonly employed in the context of the counterdiabatic driving protocol. This methodology presents a promising avenue for enhancing the efficiency of state preparation using a QLC protocol.

III. COUNTERDIABATIC DRIVE INSPIRED CONTROL HAMILTONIANS

The counterdiabatic driving protocol is a pivotal concept in non-equilibrium physics, employed to induce rapid changes in the time-dependent Hamiltonian without inducing transitions [40, 47] across instantaneous eigenstates. This phenomenon is also recognized as a “shortcut to adiabaticity” [48–51].

Consider a time-dependent Hamiltonian $H(\beta(t))$, where β represents an arbitrary function of time. When a quantum system, initially prepared in an eigenstate of the initial Hamiltonian, evolves under $H(\beta(t))$, it undergoes nonadiabatic excitations, causing it to deviate from the instantaneous eigenstate. To eliminate such transitions, a velocity-dependent term proportional to $\dot{\beta}$ is introduced to the original Hamiltonian, yielding $H(\beta) + \dot{\beta}A_\beta$. Here, A_β is defined as

$$\langle m|A_\beta|n\rangle = i\langle m|\partial_\beta n\rangle = -i\frac{\langle m|\partial_\beta H|n\rangle}{\epsilon_m - \epsilon_n}, \quad (5)$$

is known as adiabatic gauge potential with $|m\rangle$ and $|n\rangle$ being two instantaneous eigenstates of $H(\beta(t))$ and ϵ_m and ϵ_n are the corresponding time-dependent energies.

Finding an exact form of A_β for many-body quantum Hamiltonians is impractical since it requires diagonalizing the time-dependent many-body Hamiltonian. However, recently it has been shown in Ref. [52] that an approximate gauge potential can be obtained without the need for diagonalization. This approximation is constructed using nested commutators,

$$A_\beta^l = i \sum_{k=1}^l \gamma_k(t) \underbrace{[H(\beta), [H(\beta), \dots [H(\beta),]}_{2k-1 \text{ times}} \underbrace{\partial_\beta H(\beta)]]}_{\equiv H_1}, \quad (6)$$

determined by a set of coefficients $\{\gamma_1, \gamma_2, \dots, \gamma_l\}$, where l is the order of the expansion. By properly tuning these coefficients one can suppress the nonadiabatic excitations in the system. As seen from Eq. (5), the matrix elements of the counterdiabatic operator \hat{A} change sign when taking the transpose. For real matrix elements $\langle m|\partial_\beta H|n\rangle$, the operator \hat{A} is antisymmetric and purely imaginary. In this case (relevant for our work here) only odd nested commutators are [52] included in Eq. (6). For large values of l , the gauge potential incorporates long-range interacting terms. In cases where the physical Hamiltonian encompasses terms up to nearest-neighbor interactions, it

may be possible to approximate the adiabatic gauge potential solely with local and two-body interaction terms [53].

Having reviewed the counterdiabatic driving protocol, we now apply it in the context of QLC, where we introduce additional control fields inspired by counterdiabatic driving protocols. This inspiration is only in spirit and stems from the fact that the imaginary operators computed from Eq. (6) can generate fast mixing between different eigenstates. However, we note that our goal is not to make the system adiabatic. Rather, we propose to find the coefficient $\gamma_k(t)$ using multi-control QLC. Then, the resulting A_β^l may not be truly a gauge potential. The main idea here is to use the operators from the nested commutators and the coefficients from the QLC and integrate them into the quantum circuit.

The time-dependent Hamiltonian including the first control field

$$H(\beta(t)) = H_P + \beta(t) H_1, \quad (7)$$

where $\beta \equiv \beta_1$ is the control field that takes the role of β earlier. The time evolution mixes the eigenstates of H_P , with couplings $\langle n|H_1|m\rangle$ between the n^{th} and m^{th} levels. The first control Hamiltonian, H_1 , is chosen heuristically. It is inspired from quantum annealing or QAOA. It is also called a mixer Hamiltonian, in that it mixes the eigenstates of the problem Hamiltonian. Here we will consider the H_1 to be a sum of operators that act only on local qubits. For example, for the applications on the Ising model below, we will choose H_1 as a sum over Pauli- x operators which mixes across different S_z sectors.

To enhance population transfer, it is essential to devise a dynamic process that facilitates swift mixing between instantaneous eigenstates and surpasses the efficiency of the QLC with a single control parameter. To address this, we incorporate an additional control Hamiltonian into the feedback algorithm. While the potential addition of any number of control Hamiltonians are feasible in principle, our preference is to limit it to one due to the practical considerations associated with quantum circuit implementations.

To speed up transitions across wider energy intervals, one can weight transitions based on the energy differences between instantaneous eigenstates. Hence Eq. (1) with an additional control Hamiltonian H_{CD} , i.e.,

$$H_P + H_C(t) = H(\beta(t)) + \gamma(t)H_{CD}, \quad (8)$$

reads

$$i\dot{a}_n = \epsilon_n a_n + \gamma(t) \sum_m \langle n|H_{CD}|m\rangle a_m, \quad (9)$$

where we have written $|\psi(t)\rangle$ as

$$|\psi(t)\rangle = \sum_n a_n(t)|n(t)\rangle,$$

where the $|n\rangle$'s are the instantaneous eigenstates of $H(\beta(t))$. The matrix element $\langle n|H_{CD}|m\rangle$ must be dependent on the energy differences between level n and

level m . We select H_{CD} from a pool constructed by the nested commutator A_β^l in Eq. (6). The control field $\gamma(t)$ is determined by the QLC protocol described in Sec. II.

The energy differences in Eq. (9) are based on the eigenstates of the Hamiltonian $H(\beta(t))$. The control Hamiltonian H_{CD} can also be constructed from Eq. (6), by replacing $H(\beta(t))$ with the problem Hamiltonian H_P . The operator pool generated by the nested commutator constructed from H_P is a subset of the operator pool generated by Eq. (6). For practical purposes, one can use both sets of operator pools. Since we strongly truncate the series in Eq. (6) anyway, we expect both pools to have comparable performance.

IV. COUNTERDIABATIC FEEDBACK-BASED QUANTUM ALGORITHM (CD-FQA)

We enhance the FQA by introducing an additional control field inspired by counterdiabatic driving protocol. The resulting digital quantum circuit for counterdiabatic FQA (CD-FQA) discretizes the time evolution of the Schrödinger equation (1) with two control fields,

$$i \frac{d}{dt} |\psi(t)\rangle = (H_P + \beta(t)H_1 + \gamma(t)H_{\text{CD}})|\psi(t)\rangle, \quad (10)$$

where H_{CD} is an operator selected from the pool of operators inspired by counterdiabatic driving protocol. Equation (10) can be seen as specialization of Eqs. (1)-(3) for $M = 2$, with $\gamma \equiv \beta_2$ and H_{CD} a particular choice for H_2 motivated from counterdiabatic driving.

The CD-FQA quantum circuit is assembled by successively applying three unitaries,

$$|\psi_l\rangle = \prod_{k=1}^l \mathcal{U}_k |\psi_0\rangle = \prod_{k=1}^l U_{\text{CD}}(\gamma_k) U_1(\beta_k) U_P |\psi_0\rangle, \quad (11)$$

Here, $|\psi_0\rangle$ represents the arbitrary initial state, $|\psi_l\rangle$ is the quantum state after applying l layers of unitaries, and each layer is parameterized by $\{\beta_k, \gamma_k\}$. The unitaries are defined as $U_P \equiv e^{-iH_P\Delta t}$, $U_1(\beta_k) \equiv e^{-i\beta_k H_1 \Delta t}$, and $U_{\text{CD}}(\gamma_k) \equiv e^{-i\gamma_k H_{\text{CD}} \Delta t}$. For small Δt , this evolution closely resembles the continuous-time evolution of the system. The parameter Δt must be small enough so that the first-order reduction in energy must exceed all the higher-order terms [37].

The quantum circuit in CD-FQA is constructed iteratively. The unitaries U_1 and U_{CD} for the $(k+1)^{\text{th}}$ layer depend on the respective parameters β_{k+1} and γ_{k+1} . To determine these parameters, we compute the commutators $i\langle[H_1, H_P]\rangle$ and $i\langle[H_{\text{CD}}, H_P]\rangle$ using a quantum circuit for the state $|\psi_k\rangle$, i.e., a state that is built up to the k^{th} layer. Following the conventional choice for the application of QLC, we set the control fields to the following expectation values (cf. Fig. 1):

$$\begin{aligned} \beta_{k+1} &= \frac{i\alpha}{N} \langle \psi_k | [H_P, H_1] | \psi_k \rangle, \\ \gamma_{k+1} &= \frac{i\alpha}{N} \langle \psi_k | [H_P, H_{\text{CD}}] | \psi_k \rangle. \end{aligned} \quad (12)$$

Once these parameters are determined, the procedure is repeated iteratively to construct the next layer $k+2$. Since the parameters β and γ enter as prefactors to Hamiltonians, they need to scale independent of system size. This necessitates the $1/N$ scale factor in Eq. (12).

The expectation value of an operator \mathcal{O} is obtained by expanding it as a linear combination of Pauli operators, $\hat{\mathcal{O}} = \sum_i^{\tilde{N}} \gamma_i \hat{P}_i$, such that $\langle \psi_k | \hat{\mathcal{O}} | \psi_k \rangle = \sum_i^{\tilde{N}} \gamma_i \langle \hat{P}_i \rangle$ where γ_i are scalar coefficients and P_i are compact finite-size strings of Pauli basis operators. The measurement of the Pauli operators P_i is repeated to collect statistics. The resulting expectation values are combined to find the expectation value of \mathcal{O} in $|\psi_k\rangle$. The number of Pauli operators and the number of measurements will depend on the structure of H_P , H_1 , and H_{CD} . Here, we consider Hamiltonians with nearest-neighbor hopping. Therefore the number of Pauli operators is $\tilde{N} \propto N$.

The measurement of $\tilde{N} \propto N$ Pauli operators can be efficiently parallelized [54–58]. Consider, for example, the measurement of a spin Hamiltonian $\sum_i^N \sigma_i^a \sigma_{i+1}^b$ for $a \neq b$. The total number of two-qubit Pauli strings required to be measured per layer is $\tilde{N} = N$. The terms $\sigma_i^a \sigma_{i+1}^b$ and $\sigma_j^a \sigma_{j+1}^b$ can be measured simultaneously if they commute. This holds trivially if the Pauli strings do not overlap, i.e., for $|i-j| > 1$. On the other hand, overlapping, yet commuting Pauli strings share the Pauli basis operators. In the example above the number of Pauli strings can be divided into two sets containing commuting Pauli strings that act either on even or odd bonds. All Pauli strings within a set can be measured simultaneously. Consequently, the number of parallel measurements required per layer is 2. This number corresponds to the two noncommuting terms in the Hamiltonian that act on any given spin. For any counterdiabatic Hamiltonian H_{CD} , the number measurements can be obtained from the number of noncommuting terms in the commutator $[H_P, H_{\text{CD}}]$ that act on any given spin. We discuss in detail below the number of measurements needed for the LFI model with different counterdiabatic Hamiltonians and compare it with the standard FQA.

Each layer in CD-FQA comprises two parameters. In comparison with standard FQA, CD-FQA demands twice the number of measurements per layer. The circuit depth in CD-FQA is $3l$, while the circuit depth in FQA is only $2l$, where l is the number of layers. This extended depth per layer reflects the added complexity introduced by the counterdiabatic control field, emphasizing the need for enhanced computational resources per each layer in CD-FQA. Nevertheless, the incorporation of an additional control field in CD-FQA leads to a reduced number of layers in CD-FQA. For a small number of layers our algorithm shows tremendous improvement over standard FQA.

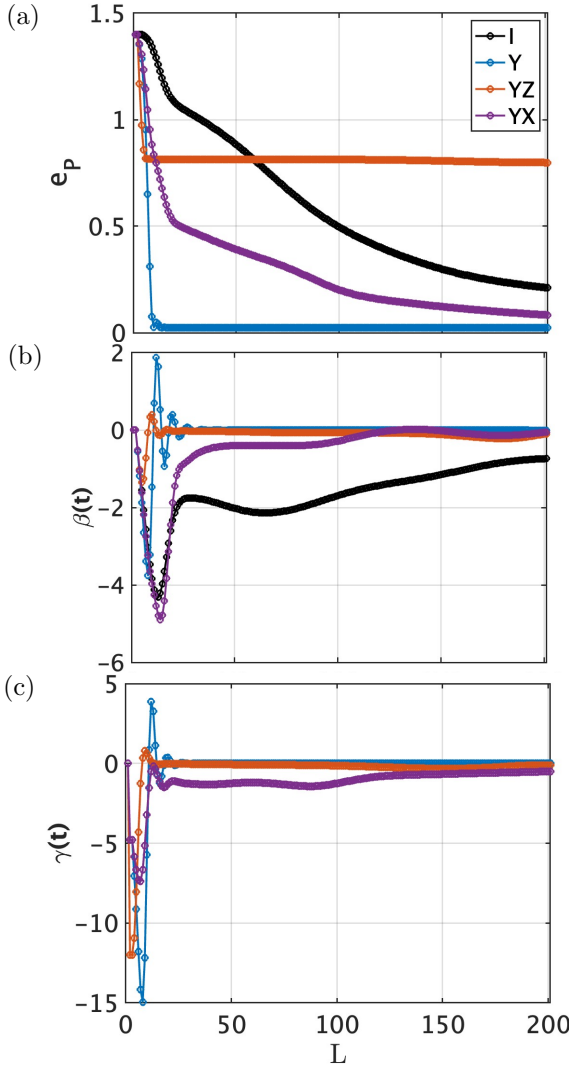


FIG. 2. (a) The average energy per site is shown as a function of the number of layers for LFI ($h_z = 0.4$, $h_x = 0$) with $N = 6$ spins for various CD-FQA protocols. The black color represents the standard FQA which is equivalent to taking the identity for H_{CD} , i.e., $H_{\text{CD}} = I$ as indicated in the legend. The other colors represent CD-FQA with a particular operator denoted by H_{CD} selected from the pool (14). (b) The first and (c) the second control fields, $\beta(t)$ and $\gamma(t)$, respectively, are shown as a function of the number of layers for different H_{CD} . Parameters $\alpha = 6$ and $\Delta t = 0.01/J$.

V. RESULTS: PREPARING THE GROUND-STATE OF ISING SPIN MODELS

We apply the CD-FQA to Ising chains of length N

$$\begin{aligned} H_I &= \sum_i^N \left(-J\sigma_i^z\sigma_{i+1}^z - h_z\sigma_i^z - h_x\sigma_i^x \right) \quad (13) \\ &\equiv -ZZ - h_z Z - h_x X, \end{aligned}$$

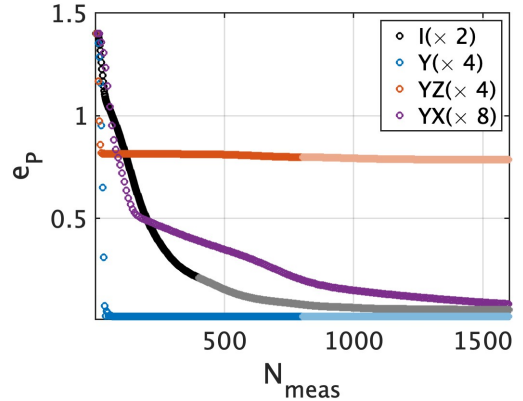


FIG. 3. The average energy per site for LFI vs. number of parallel measurements up to repeats. Same data as in Fig. 2, yet plotted vs. the number of measurement layers N_{meas} . Because the number of parallel measurements per layer varies across different CD-FQA protocols, this applies different horizontal scale factors to the data in Fig. 2(a) as indicated with the legend here. The darker sections of each curve correspond to the $L = 200$ layers in Fig. 2.

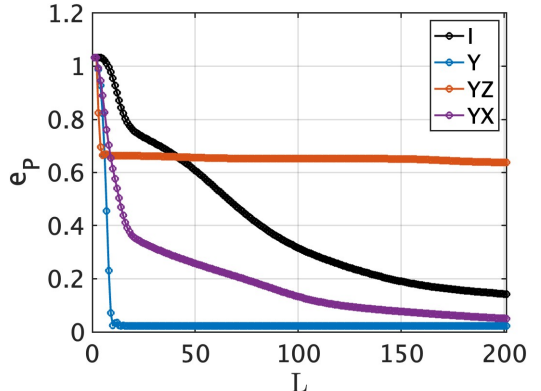


FIG. 4. The average energy per site is shown as a function of the number of layers for MFI ($h_z = h_x = 0.4$). All other parameters are same as Fig. 2.

and for various parameter settings. The nearest-neighbor interaction $J := 1$ sets the unit of energy, throughout, while h_z and h_x specify the longitudinal and transverse fields, respectively. The operators σ_i^a with $a \in \{x, y, z\}$ are the standard Pauli operators acting on site i . We use periodic boundary conditions (PBC) in all classical simulations except for Fig. 12 where we use open boundary conditions (OBC) for quantum simulation. For convenience, we employ shorthand notations to describe the sums of Pauli operators. The sum of local operators is denoted by $A \equiv \sum_i^N \sigma_i^a$, with $A \in \{X, Y, Z\}$ corresponding to $a \in \{x, y, z\}$, respectively. Similarly, two-body terms are denoted by $AB \equiv \sum_i^N \sigma_i^a \sigma_{i+1}^b$. With this, the Hamiltonian in Eq. (13) can be written as shown in the line below it.

By varying the parameters h_z and h_x , we investigate

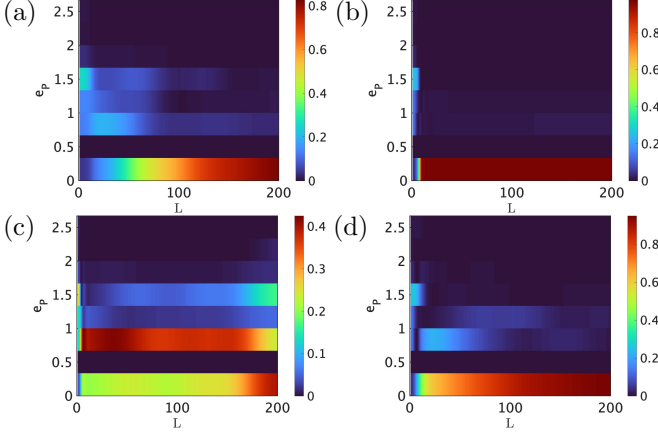


FIG. 5. Binned energy distribution of the state ψ vs. circuit depth for the MFI for the simulation of Fig. 4. The panels represent CD-FQA protocols with operators (a) I (i.e., plain FQA), (b) Y , (c) YZ , and (d) YX , respectively. The average energies per site e_P are coarse-grained into 8 bins of equal width $2J$. For each circuit depth, the energy densities integrate to 1 vertically over all energies.

four distinct types of Ising models: (i) longitudinal field Ising (LFI) when $h_x = 0$, (ii) transverse field Ising (TFI) when $h_z = 0$, (iii) mixed-Field Ising (MFI) with non-zero values for all parameters, and (iv) A special case $h_x = h_z = 0$. This study showcases the versatility of the CD-FQA approach in tackling various Ising models with different field configurations.

In all considered cases, the first control Hamiltonian is defined as $H_1 = X$. This Hamiltonian, commonly referred to as a mixer Hamiltonian, is a standard choice in QAOA and quantum annealing protocols, particularly when the problem Hamiltonian consists of Z terms. Here, we set the initial state to be the ground state of $-H_1$ $|\psi_0\rangle = |X\rangle \equiv |-\rightarrow \dots \rightarrow\rangle$, where all spins are aligned along the x -axis. This initial state, being a product state, can be readily prepared on a quantum circuit using only Hadamard gates. Equivalently, $|X\rangle = e^{-i\frac{\pi}{4}Y}|Z\rangle$ with $|Z\rangle \equiv |+Z\rangle \equiv |\uparrow \uparrow \dots \uparrow\rangle$.

The second control Hamiltonian in our approach draws inspiration from the counterdiabatic protocol as discussed in Sec. III, and is selected from an operator pool generated by the nested commutator Eq. (6). Importantly, we restrict the operator pool to include only local and two-body terms. When the problem Hamiltonian and the first control Hamiltonian are real then the operator pool comprises solely operators with imaginary matrix elements. The counterdiabatic operator pool A_{pool} is a subset of the operator pool consisting of all the local and two-body operators and is given by

$$A_{\text{pool}} \subseteq H_{\text{pool}} = \{Y, ZY, YZ, XY, YX\}. \quad (14)$$

The terms in Eq. (14) are generated by commuting individual terms of $H_P = H_I$ with $H_1 = X$. As it turns out,

YZ and ZY exhibit identical behavior, similar to YX vs. XY . With this, we eliminate ZY and XY from the pool above. Yet for the sake of the presentation, we include the identity I to the pool, which then simply represents the standard FQA.

A. $h_z \neq 0$ (LFI and MFI)

First, we consider the case of non-zero longitudinal field $h_z = 0.4$ where we find that both LFI ($h_x = 0$, Fig. 2) and MFI ($h_x = h_z$, Fig. 4) yield similar results. The system consists of $N = 6$ spins, and the simulation is performed up to 200 circuit layers using $\Delta t = 0.01$. The parameter α in the QLC protocol is assumed to be 6, so that the prefactor $\alpha/N = 1$.

We depict three distinct CD-FQA protocols, each associated with a different operator selected from the pool, characterized by $H_{\text{CD}} \in \{Y, YZ, YX\}$. These are derived from terms that arise from the nested commutators (6), Y and YZ at first order, and YX at second-order. The performance of CD-FQA, for each choice of H_{CD} , is compared against the standard FQA represented by the black curves.

In Fig. 2a we plot the average energy per site relative to the ground state energy E_0^P of H_P ,

$$e_P \equiv \frac{1}{N} (\langle H_P \rangle_t - E_0^P) \quad (15)$$

against the number of circuit layers. While, by construction, all four curves show monotonic decay, there are significant qualitative differences. The CD-FQA approaches demonstrate a strongly accelerated reduction of the energy at early times, i.e., small number of layers. However, with an increasing number of layers, the CD-FQA protocol associated with YZ shows early plateau-like behavior, thus failing to decrease the energy to E_0 . We find that the CD-FQA with Y achieves the most favorable results, followed by the YX protocol. These findings highlight the effectiveness of CD-FQA in the ground-state preparation, yet also reveal clear differences depending on the choice of the operator for H_{CD} .

The control fields $\beta(t)$ and $\gamma(t)$ are presented in Fig. 2b and Fig. 2c. Starting from zero, these fields decrease rapidly towards a minimum, before returning to zero at large times with an irregular oscillatory intermediate behavior. The initial changes in $\gamma(t)$ [Fig. 2c] strongly surpass those in $\beta(t)$ [Fig. 2b], thus contributing to a significantly more rapid decay in average energy as compared to standard FQA. The control fields in the CD-FQA with Y and YZ reach zero within a short time, while in the standard FQA and CD-FQA with YX they have sizeable value over a significantly longer times.

The number of measurements is a key resource in our protocol. As we have established, the number of measurements per layer without repeats equals the number of non-commuting Pauli strings acting on any site. For the LFI model the commutator $[H_P, H_1]$ yields terms $YZ + ZY$ and Y . The term $\sigma_i^y \sigma_{i+1}^z$ commutes with

$\sigma_j^z \sigma_{j+1}^y$ for $j = i \pm 1$. Therefore they can be measured simultaneously. With this, the number of parallel measurements needed to find expectation values of $YZ + ZY$ and Y is 2, since measuring $YZ + ZY$ is enough to extract information about the Y -measurement. Similarly for the CD-FQA protocol, with $H_{CD} = Y$, the commutator $[H_P, H_{CD}]$ yields terms $\{X, XZ, ZX\}$. Again this requires 2 parallel measurements, adding up to a total of 4 measurements per layer. For $H_{CD} = YZ$, the commutator $[H_P, H_{CD}]$ yields $\{X, ZXZ, XZ\}$. This also requires 2 parallel measurements per layer, adding up to a total of 4 parallel measurements for that protocol. For $H_{CD} = YX$, the commutator $[H_P, H_{CD}]$ yields $\{XY, YYZ, ZXX, XX, YY\}$. Since the expectation values for $YZ + ZY$ and Y out of $[H_P, H_1]$ can be obtained from the data for this set, the protocol requires a total of 8 parallel measurements per layer. In Fig. 3, we plot the average energy per site vs number of measurements required for different CD-FQA protocols. The number of measurements in the protocol with Y as a CD operator converges much faster than other protocols. The protocol with YX as a CD operator requires more measurements per layer as compared to standard FQA. Therefore the measurement cost between different protocols depends on the degree of locality in the system. We emphasize, however, that the number of parallel measurements is *independent* of the system size for any protocol.

We repeat the same simulation as in Fig. 2 but this time also with $h_x = 0.4 (= h_z)$ turned on (MFI). The data presented in Fig. 4 is very similar to Fig. 2a, except that the system starts out a somewhat lower energy in the system when adding the transverse term.

The key distinction between the LFI and MFI models lies in the additional X term present in the problem Hamiltonian. Since $H_1 = X$, the introduction of the X term in H_P has minimal influence on $\beta \sim \langle [H_P, H_1] \rangle$. On the other hand, $\gamma \sim \langle [H_P, H_{CD}] \rangle$ does acquire additional terms. However, given that the initial state is the ground state of X , these contribute insignificantly to the rates γ at early times since for the transverse term X in H_P , $\langle [X, H_{CD}] \rangle \sim 0$. Further discussions on the rate of energy change and its dependence on various commutators and the initial state are elaborated in Sec. VII in the context of different CD-FQA protocols.

The emergence of plateaus in Fig. 2a and Fig. 4 raises questions on the nature of the ‘steady’ state reached. In the worst case, the system might converge to an excited eigenstate of H_P , in which case also $\beta, \gamma \rightarrow 0$. Hence in order to gain deeper insights into the impact of CD-FQA on ground state preparation, Fig. 5 tracks the energy distribution in the system vs. circuit depth with respect to the eigenspectrum of H_P . For this purpose, we partitioned the full many-body energy window into eight bins. The general behavior in Fig. 5 largely aligns with those in Fig. 4. In the standard FQA [Fig. 5a], the population gradually transfers to the ground state, reaching approximately a weight of $p_0 \sim 0.825$ in the lowest bin, where p_i is the overlap of the wavefunction with all the eigenstates

in the $(i - 1)^{\text{th}}$ bin. In contrast, the Y-FQA protocol achieves $p_0 \sim 0.976$ within just a few layers. Similarly, the YX-FQA protocol, in agreement with the results in Fig. 4a reaches $p_0 \sim 0.948$.

The YZ-FQA protocol [Fig. 5c] notably fails to reach the ground state with $p_0 \sim 0.398$. This is consistent with the plateau observed in Fig. 4a for YZ-FQA. However, as seen with the energy resolution here, by having considerable weight at low energy, the energy distribution remains broad, overall. Therefore the CD-FQA protocol does not drive the state into an excited eigenstate. Instead, several eigenstates of H_P over a wider energy window conspire to form an approximate steady state for the FQA protocol. Despite the variations vs. circuit depth in the energy distribution, the average energy in the system barely changes. For example toward the largest times (circuit depth), there are three bins with pronounced weight (p_0 , p_2 , and p_4). While p_0 gains weight, for $l \gtrsim 175$, so does p_4 , at the cost of the intermediate energy bin p_2 . Therefore overall, the energy expectation value remains nearly the same.

So far, we have illustrated the behavior of CD-FQA protocols for different second-control Hamiltonians while keeping all the other parameters fixed. In the following paragraphs we present the effect of CD-FQA protocols for different values of α , systems size N , and the time-step Δt .

1. CD-FQA for different values of α

The parameter α assumes a pivotal role in the CD-FQA protocol, as shown by the proportional relationship between the rate of change of average energy and α in Eq. 4. The dependency of α on the protocol for arbitrary circuit depth, however, is non-trivial. Our findings are presented in Fig. 6, where the average energy is plotted against circuit depth for four distinct values of α . In the context of standard FQA [Fig. 6a] a larger α induces a rapid reduction in energy for shallow circuit depths, while for large circuit depth the protocol with a smaller α demonstrates superior convergence. Notably, in the CD-FQA protocol with Y [Fig. 6b], performance improves with increasing α . However, beyond a certain value of α , the average energy exhibits pronounced oscillations, failing to decrease after a few layers. Similar behaviors are observed in CD-FQA with YZ and YX [Figs. 6c and d, respectively]. The monotonic decrease of the energy is guaranteed in Eq. (3) only for the differential setting with infinitesimally small Δt . Hence the onset of oscillations in the energy, where the energy also intermittently increases, is necessarily due to the finite Δt chosen. Figure 6 thus suggests an upper limit $\alpha \Delta t \lesssim 0.1/J$, above which Eq. (3) fails to decrease energy (see Fig. 8 for a more detailed analysis still). This underscores the importance of α together with Δt in governing the performance dynamics of CD-FQA protocols, providing valuable considerations for the optimized CD-

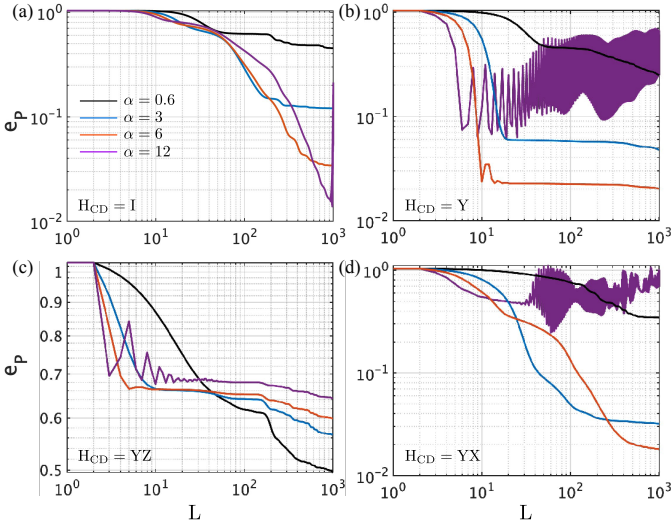


FIG. 6. Average energy difference per site shown as a function of circuit depth in log-scale for the MFI model for various α as specified in the legend in (a) for all panels, having $N = 6$, $\Delta t = 0.01/J$. Each panel corresponds to a different CD-FQA protocol for the H_{CD} as specified.

FQA protocol for a given quantum circuit depth.

2. CD-FQA for different system sizes

In Fig. 7, we present a comprehensive analysis of energy reduction versus circuit depth across a range of system sizes ($N = 4$ to $N = 10$) using various CD-FQA protocols, maintaining a fixed $\alpha = 4$. The results depicted in all four figures underscore the *robustness* of the CD-FQA protocol, demonstrating its independence from system sizes up to 100 layers where $L\Delta t \sim 1$. Deviations in the curves for $N = 4$ and $N = 5$ are attributed to the influence of small system size. A noteworthy comparison can be drawn with the findings in Ref. [36], where the authors establish a linear relationship between the number of layers and system sizes. It is crucial to highlight a key distinction: unlike the approach in Ref. [36], our methodology involves normalizing the prefactor, as illustrated in Eq. (4). Here, the parameters β and γ are normalized by a factor of N . For large circuit depth, on the other hand, we find across all panels in Fig. 7 that the smaller system sizes show a somewhat improved performance. This may be attributed to the larger finite-size level spacing within the excited states.

The observed independence of the circuit depth for the above case is due the finite correlation length of the system bearing in mind that the system is gapped. This has the advantage that one can use the results of small sizes as an insight to design the protocol for large sizes. Another relevant comparison can be drawn with the findings in Ref. [41], where the authors, employing a Reinforcement Learning method, observed similar independence of

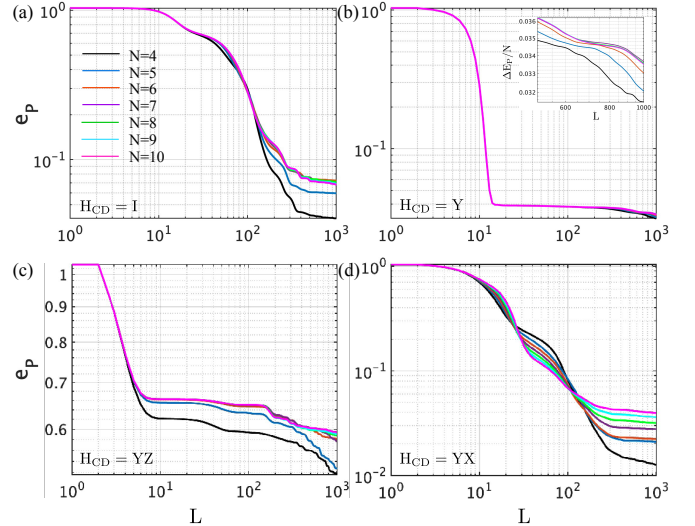


FIG. 7. Average energy difference shown as a function of circuit depth in log-scale for the MFI model for various values of N as specified in the legend in (a) for all panels, having $\alpha = 4$, $\Delta t = 0.01/J$. Each panel corresponds to a different CD-FQA protocol for the H_{CD} as specified. The inset in (b) demonstrates the large-time behavior.

the number of layers on system sizes in a QAOA-type architecture. In their study, unitaries composed of the MFI Hamiltonian, X , and Y were strategically ordered using a policy derived from Reinforcement Learning techniques. The signature that the number of layers in a CD-FQA circuit is nearly independent of the system size for the MFI model highlights the practical usage of such a protocol for large-system sizes.

3. CD-FQA for different time-steps Δt

Finally, we also analyze the dependence of the CD-FQA protocols on the value of Δt . Larger Δt leads to a shallower circuit depth which is desirable for the implementation in a quantum circuit. Too large a Δt , however, can lead to a deviation from the QLC protocol that results in an energy increase in Eq. (3). In Fig. 8 we present the average energy decay as a function of the total simulated time $T \equiv L\Delta t$ for four values of Δt . For $\Delta t \gtrsim 2\tau$, and therefore $\alpha\Delta t \gtrsim 0.1/J$, the CD-FQA protocol starts to oscillate after a few layers and the average energy does not decrease with circuit depth. The limit on Δt to describe the differential setting in Eq. (3) is thus comparable to what one may use in a Trotterized setting, bearing in mind that α enters as a scale factor to the full Hamiltonian in Eq. (1). Nevertheless, since we are not interested in the trajectory of the prepared state per se, but only in the final result, in principle, this opens the possibility to use adaptive Δt along the circuit starting from larger values. We leave this additional fine-tuning as an outlook for future studies. For the present paper, however,

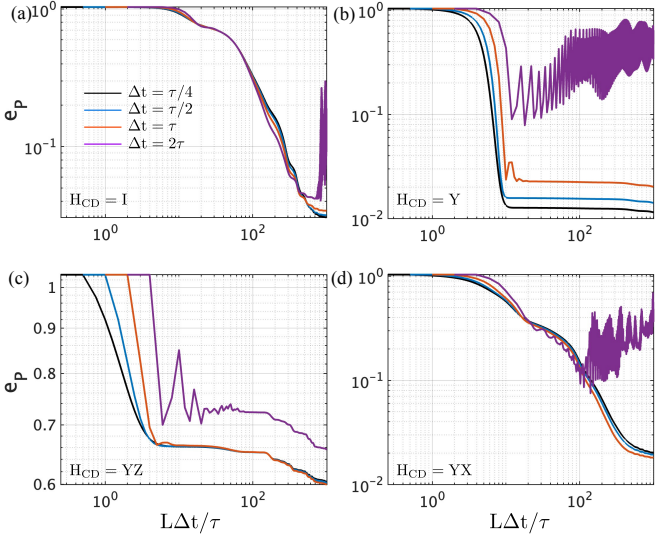


FIG. 8. Average energy difference shown as a function of circuit depth in log-scale for the MFI model for various Δt relative to the constant $\tau = 0.01/J$ used previously, with values specified in the legend of (a) for all panels, having $N = 6$, and $\alpha = 6$. Each panel corresponds to a different CD-FQA protocol for the H_{CD} as specified. Panel (c) demonstrates the early plateau behavior.

we keep Δt constant throughout the circuit.

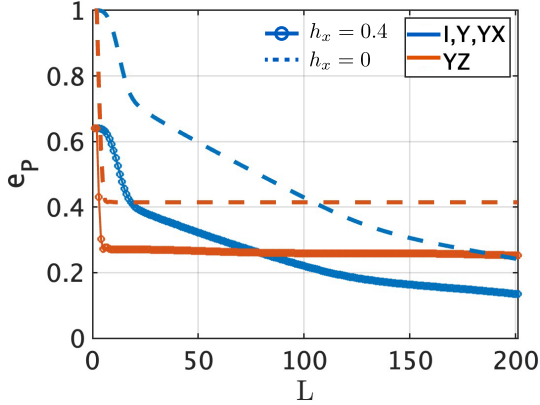


FIG. 9. Average energy vs. circuit depth for TFI with $h_x = 0.4$ (solid lines) and $h_x = 0$ (dashed lines). The standard FQA and CD-FQA with $H_{CD} = Y$ and YX yield the same result.

B. TFI (including $h_x = 0$)

Now we apply the CD-FQA protocols to Ising chains with the longitudinal field turned off, i.e., $h_z = 0$, with the results presented in Fig. 9 for $h_x = 0.4$, and $h_x = 0$. The ground state of the TFI is in the ferromagnetic phase and at $h_x = 0$ there are two degenerate ground states $|\psi_{g1}\rangle = |\uparrow \dots \uparrow\rangle$ and $|\psi_{g2}\rangle = |\downarrow \dots \downarrow\rangle$.

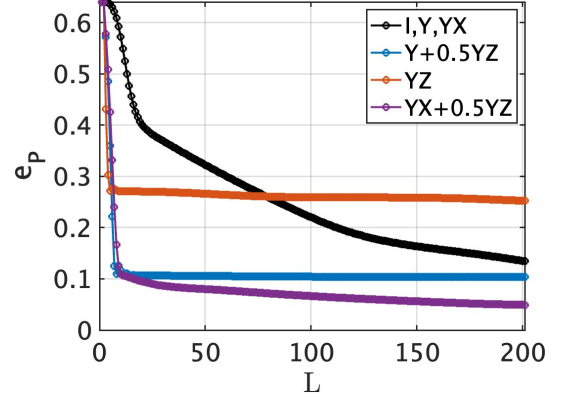


FIG. 10. Average energy vs. circuit depth for TFI with $h_x = 0.4$ with CD-FQA operator is a linear combination of two operators from the pool.

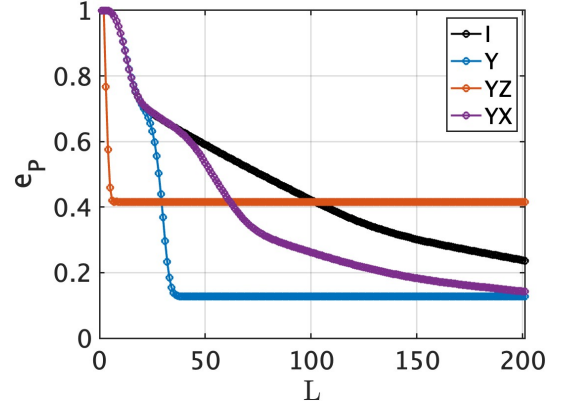


FIG. 11. Average energy vs. circuit depth for the TFI at $h_x = 0$, but now including the term $H_{\text{add}}(k) = e^{-(k-1)/5} Z$ for layer k .

The CD-FQA protocol employing the $H_{CD} = YZ$ operator demonstrates a rapid energy reduction initially but becomes exceedingly slow as we increase the number of layers, exhibiting a plateau similar to the ones seen for LFI and MFI. This protocol fails to reach the ground state, rendering it undesirable. Notably, CD-FQA with $H_{CD} = Y$ and YX mirrors the outcomes of the standard FQA, since $\gamma = 0$ for all time steps.

In situations where the CD-FQA faces challenges in convergence such as in Fig. 9 one may consider various approaches to improve the performance of the protocol. For instance, one may choose H_{CD} as a linear combination of operators from the pool of operators or add a small time-dependent Hamiltonian that vanishes at the end of the protocol.

1. Improving CD-FQA with linear combination of operators

To address the limitations of the YZ operator in the TFI model, we first introduce the counterdiabatic oper-

ator as a linear combination of two operators from the operator pool. In Fig. 10, we plot the CD-FQA protocol with $H_{CD} = Y + \frac{1}{2}YZ$ and $YX + \frac{1}{2}YZ$ together with $H_{CD} = YZ$ and the standard FQA. The combination of these imaginary operators promotes a better mixing between instantaneous eigenstates compared to individual operators from the pool. As depicted in Fig. 10 the CD-FQA protocol with linear combination achieves a rapid decrease in average energy, surpassing the energy obtained with the YZ term alone. Although employing a linear combination of multiple counterdiabatic operators circumvents the plateau observed with a single counterdiabatic operator, the implementation on a quantum circuit requires more than a single layer. A similar linear combination of operators have been utilized as a counterdiabatic term in Ref. [59] in the digitalized counterdiabatic quantum optimization for MFI model.

2. Improving CD-FQA with an additional time-dependent Hamiltonian

Another viable strategy to improve the CD-FQA is to introduce a time-dependent term into the dynamics. It is crucial to configure the time dependence of the additional term in a manner such that the magnitude of the term gradually diminishes throughout the protocol, ultimately reaching zero upon the protocol's completion. Furthermore, the additional term must commute with the problem Hamiltonian so that the protocol does not introduce additional measurement for β and γ .

Let us illustrate this approach with a specific example, considering the case where $H_P = -ZZ$ and $H_1 = X$. As previously demonstrated, the counterdiabatic protocol with YZ fails to converge to the ground state, resulting in the average energy plateauing at a value higher than the ground state. To address this, we introduce a commuting time-dependent term, denoted as $H_{\text{add}} = f(t_k)Z$, where t_k corresponds to the time at the k^{th} layer. The modified total time-dependent Hamiltonian is now expressed as $H(t) = H_P + H_{\text{add}}(t) + \beta(t)H_1 + \gamma(t)H_{CD}$. The QLC protocol continues to be determined by the condition $d\langle H_P \rangle / dt \leq 0$. However, the introduction of $H_{\text{add}}(t)$ alters the effectiveness of counterdiabatic operators, allowing the utilization of Y as H_{CD} for constructing the CD-FQA protocol. In Fig. 11, we present the average energy as a function of the number of layers, incorporating the additional term and selecting $H_{CD} = Y$. The CD-FQA protocol with the additional term exhibits better performance compared to the protocol with the YZ operator.

It is important to note that the introduction of the Z term breaks the degeneracy of the ground state of $H_P = -ZZ$ as well as some of the excited states. Depending on the sign of the Z , the CD-FQA converges to a state closer to one of the degenerate states within the ground state manifold. Indeed, in our protocol, if it were not for the Z , the state would be forced to flow to the GHZ state, which

is known to have a linear circuit complexity [60, 61], since both the initial state and the unitaries in CD-FQA are symmetric under $\prod_j X_j$.

To see this, recall that we start with an initial state $|+X\rangle$, and both H_P and H_1 commute with $\prod_j X_j$. Operators from nested commutators (i.e., the YZ operator) also commute with $\prod_j X_j$. Since we minimize the energy of $H_P = ZZ$, when we are restricted to the $\prod_j X_j = 1$ subspace, we are forced to flow to GHZ. An additional Z term in the Hamiltonian biases the system towards either $|+Z\rangle$ or $|-Z\rangle$ and breaks away from the symmetry subspace. This addition of Z further allows us to utilize Y as a second control Hamiltonian. So one possible strategy to expedite conversion to a ground state is to select a symmetry-breaking operator as the additional term when an obstruction due to long-range order is expected.

Both strategies employed above highlight the importance of alternate approaches to tweak the CD-FQA protocol to navigate the quantum landscape effectively. However, one must take into account that the introduction of an additional Hamiltonian always increases the number of gates and thereby the depth of the quantum circuit.

Furthermore, in Appendix A, we extend our investigation for the TFI by exploring an alternative first control Hamiltonian, specifically $H_1 = Z$, and the corresponding initial state $|\psi_0\rangle = |\uparrow\uparrow\dots\uparrow\rangle$. The CD-FQA under this configuration exhibits superior performance compared to the scenario shown in Fig. 9. All three counterdiabatic operators demonstrate better performance in achieving ground-state compared to the standard FQA. Consequently, it is evident that the choice of H_1 significantly impacts the CD-FQA's performance in the context of the TFI. In this comparison, Z emerges as a more favorable first control Hamiltonian than X for the TFI, highlighting the importance of the specific control Hamiltonian selection in the CD-FQA.

VI. DEMONSTRATION ON CLOUD QUANTUM COMPUTERS

To showcase the enhanced performance of CD-FQA over FQA on an actual quantum platform, we conducted demonstrations on IBM's superconducting quantum computer through cloud-based simulations, employing CD-FQA for the MFI with a four-spin system with OBC for parameters $h_x = h_z = 0.4$. As we set a small time step interval $\Delta t = 0.02$, we find that one-layer Trotterization (e.g. $e^{i(ZZ+X)} \approx e^{iZZ}e^{iX}$) suffices for an accurate simulation. The experiment is done recursively. We use the k -step circuit to measure the commutators (i.e. expectation values of each Pauli term in the commutators), and get $\beta_{k+1}, \gamma_{k+1}$ for the circuit of next step. The outcomes, illustrated in Fig. 12, reveal a consistent monotonic decay of energy in FQA and YX-FQA up to the 9th layer. Conversely, in the Y case, we observed a decrease only up to the 5th layer, and YZ failed to exhibit

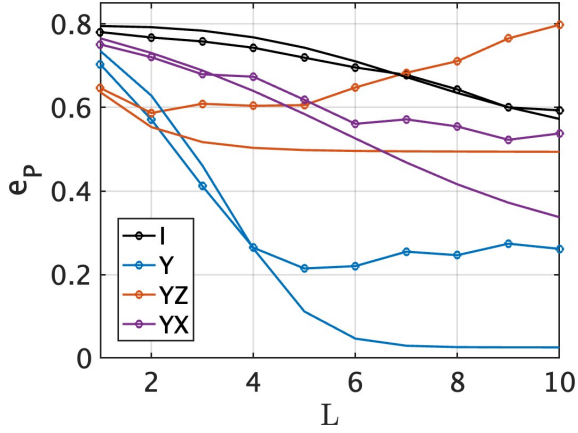


FIG. 12. The average energy is shown as a function of the number of layers for 4-qubit MFI with $h_z = h_x = 0.4$ and $\Delta t = 0.02$. The simulation is performed on `ibm_torino` with 28 192 repetitions for each measurement. The curves with markers represent data from quantum computers while the solid lines represent classical simulations.

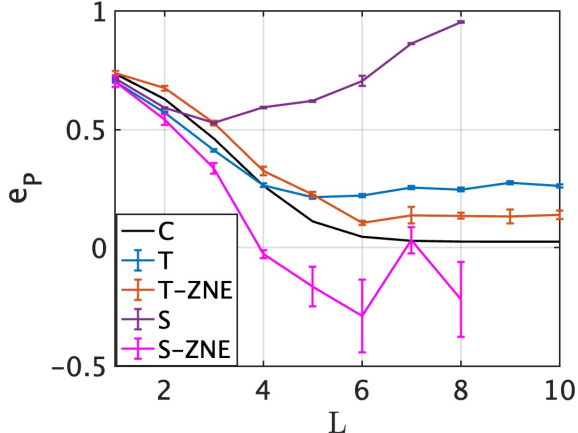


FIG. 13. The experimental results from IBM_Torino (T), IBM_Sherbrooke (S), and IBM_Sherbrooke with zero-noise extrapolations (S-ZNE) is compared with the classical simulation (C) for the CD-FQA with Y as the CD-operator. The average gate error per layer for IBM_Torino is 0.8%, and 1.7% for IBM_Sherbrooke, thus resulting in the deviations observed for $L = 1$. All other parameters are same as in Fig. 12. The deviations of the energies for the four curves at $L = 1$ are from below 1% to around 5%, with T-ZNE having the best accuracy and S the worst.

any decay even in the second layer.

Considering the impact of gate noise inherent in quantum circuits, deploying a substantial number of 2-qubit gates resulted in undesirable outcomes. Therefore, in conventional FQA and CD-FQA utilizing the Y operator, where local operators are employed as H_1 and H_{CD} , we found such circuits demonstrated a decrease in energy performance up to the 6th layer. Moreover, the CD-FQA

with Y performs the best. The state generated after the application of numerous layers exhibited an undesirable growth in energy, a phenomenon unsuitable for any protocols. The influence of noise became evident in measurements, where all Pauli operator expectation values approached zero. Nevertheless, for a limited number of layers, we observed an enhancement of CD-FQA over conventional FQA in terms of both energy accuracy and convergence speed, particularly in the case of Y-FQA. Below we discuss the effect of gate noise and methods to improve experimental results. The discussion on statistical errors that may appear due to the measurements is discussed in the Appendix C.

A. Improving results from IBM's cloud quantum computers

The experimental data in Fig. 12 deviates from the classical simulations. The primary reason for such discrepancy stems from the limitations of the current NISQ devices. Gate errors accumulate exponentially with circuit depth L . In Fig. 13 we compare the quantum simulations performed on IBM_Sherbrooke with the newer IBM_Torino system. The energy curve obtained from the IBM_Sherbrooke for Y-FQA deviates significantly from the theoretical curve already for $L > 3$. To improve this discrepancy one can use either a less noisy machine, or error mitigation schemes such as zero-noise extrapolation (ZNE) [62, 63]. As shown in Fig. 13, curves obtained from both machines get closer to the theoretical one after applying ZNE. The average gate error per layer for IBM_Sherbrooke is around 1.7%, while the rate for IBM_Torino is 0.8%. Thus the data from IBM_Torino is more accurate and consistent with the theoretical curve up to $L = 5$. In the ZNE approach of Ref. [63], the circuit, created by the overall unitary U , is ‘folded’ by looking at a sequence of equivalent unitaries, $UU^\dagger U$, $UU^\dagger UU^\dagger U$, $\dots = U(U^\dagger U)^n$. Since the noise gets amplified with increasing n , this then permits an extrapolation to a zero-noise limit. While the method can achieve better accuracy for expectation values, at the same time it may also increase the uncertainty of the results, as seen in Fig. 13.

VII. DISCUSSION

An important aspect of CD-FQA lies in the strategic selection of the additional control Hamiltonian, H_{CD} , within the given context of the provided H_P and H_1 . This choice significantly influences the evolution of the control field $\gamma(t) \propto \langle [H_P, H_{CD}] \rangle$ which depends on both, the commutator and the state $\psi(t)$. In our investigation with $H_1 = X$, the initial state is chosen as the ground state of $-H_1$, $|\psi_0\rangle = |X\rangle \equiv |\rightarrow\rightarrow\dots\rightarrow\rangle$. As this extremizes $\langle X \rangle$, a strategy to enhance the energy reduction via $\gamma \sim \langle [H_P, H_{CD}] \rangle$ at early times is to look

for operators H_{CD} that yield $[H_P, H_{CD}] \sim X$. Given our initial state, therefore the commutators resulting in X or XX lead to the largest γ 's at early times. This leaves only a few choices for H_{CD} :

$$H_{CD} = Y \quad (16a)$$

$$H_{CD} = YX \text{ or } XY \quad (16b)$$

$$H_{CD} = YZ \text{ or } ZY \quad (16c)$$

since for Eq. (16a), $[(H_P \rightarrow Z), Y] \sim X$, for Eq. (16b), e.g., $[(H_P \rightarrow Z), YX] \sim -XX + YY$. For these to occur, this also shows the importance of the longitudinal term Z in H_P to be present. The last option in Eq. (16c) arises since, e.g., $[(H_P \rightarrow ZZ), YZ] \sim -XZZ - ZXZ$ where the diagonal terms in ZZ lead to X . In all cases, H_{CD} needs to include Y . This makes intuitive sense, since Y is required to rotate the initial state $|X\rangle$ to $|Z\rangle$ which is close to the Ising ground state, exactly so for $h_x = 0$.

In the presence of the Z term in the Hamiltonian (LFI and MFI) all three counterdiabatic operators in Eqs. (16) exhibit a rapid reduction in average energy values over a small number of layers. As seen in Figs. 2 and 4, the best performance for long times is given by $a > b > c$ [based on the subequation numbering in (16)]. Notably, the one with the worst long-term performance (c) demonstrates the fastest energy reduction at early times. This shows that focusing solely on the most rapid energy reduction in the choice of H_{CD} can drive the system into barren plateaus in terms of quasi-steady states at elevated energy [cf. Fig. 5c].

In stark contrast, in the absence of the Z term in the Hamiltonian (TFI, including $h_x = 0$), only the option in Eq. (16c) remains in order to effectively reduce the energy, as also seen in Fig. 9. In this case, using Eq. (16a) has no effect whatsoever, with the data identical to plain FQA. Similar to the LFI case, however, the YZ operator is prone to getting stuck at finite energy. As seen in Fig. 9, adding YX , while irrelevant at early times, nevertheless does permit to drive the system to lower energy after the initial stage.

We have also addressed variations of the CD-FQA protocol to overcome the early plateaus seen in Fig. 9. The two approaches involve incorporating a linear combination of two operators from (16) or adding a time-dependent term to the H_P that diminishes over time. Such variations yield excellent results for the TFI.

Feedback-based quantum algorithms require a deep circuit with many layers and are beyond the scope of the current NISQ devices. However, a shallow FQA circuit can be utilized to “warm start” a QAOA-type quantum circuit, i.e., to use the FQA parameters β_k to initialize the QAOA algorithm. Note that, each layer in QAOA is parametrized by two real numbers, and one of the parameter is 1 and the second parameter is approximated by β_k . We observe that a similar extension is also possible for the CD-FQA, where one can utilize the parameters of CD-FQA circuit to warm start a VQA, where each layer

is parameterized by three layers. This translates to a digitalized-counterdiabatic inspired QAOA [42] where the initial parameters are selected from the CD-FQA.

VIII. CONCLUSION

In this study, we have extended the FQA by incorporating the principles of QLC with the counterdiabatic driving protocol. Departing from the conventional use of a single control field, we propose the integration of a second control field inspired by the counterdiabatic driving protocol. This modification proves instrumental in accelerating ground state preparation, showcasing its effectiveness for implementation on digital quantum circuits. The CD-FQA has been systematically applied to four distinct variants of the Ising models. Our results showcase the intricate interplay between various parameters involved in the CD-FQA and how a proper selection of the second control Hamiltonian depends on the problem Hamiltonian, first control Hamiltonian, and the initial state for fast preparation of the ground state. On the one hand, the introduction of a second control field contributes to an increase in complexity within a single layer. On the other hand, this effectively reduces the overall circuit complexity. These two system-dependent aspects need to be balanced for optimal performance. The parameters of the presented FQA can serve as an initial seed for further classical optimization. This opens the potential for extending the CD-FQA parameters to set up QAOA circuits, thus allowing one to combine quantum and classical optimization methodologies. This is particularly noteworthy, as previous research has successfully demonstrated a three-unitary QAOA utilizing a similar operator pool [42]. Beyond its applications in quantum optimization algorithms, the CD-FQA unveils novel possibilities in the realm of fast quantum control methods employing counterdiabatic driving protocols. This convergence of quantum algorithmic advancements and control theory holds promise for shaping the future landscape of quantum computing. In conclusion, our work not only enhances the understanding of ground state preparation in quantum many-body systems but also adds insights for quantum control strategies with far-reaching implications in the field.

IX. ACKNOWLEDGMENTS

The authors thank Ning Bao and Ananda Roy for useful discussions. All authors of this work were supported in its production by the U.S. Department of Energy, Office of Basic Energy Sciences, under Contract No. DE-SC0012704. TCW acknowledges the support of an SBU Presidential Innovation and Excellence (PIE) Fund. This research also used resources from the Oak Ridge Leadership Computing Facility, which is a DOE Office of Science User Facility supported under Contract DE-AC05-

00OR22725, and the Brookhaven National Laboratory operated IBM-Q Hub. The results presented in this work do not reflect the views of IBM and its employees.

Appendix A: CD-FQA for the TFI: additional plots

In Fig. 14, we apply the CD-FQA protocol to two TFI models where $H_1 = Z$ serves as the first control Hamiltonian, coupled with the initial state $|\psi_0\rangle = |\uparrow\uparrow\dots\uparrow\rangle$. Unlike the results observed in Fig. 9, where the CD-FQA with Y and YX aligns with the standard FQA, the CD-FQA protocols in Fig. 14 yield different curves for the average energy. The contrast between the two figures underscores the significant impact of the first control Hamiltonian on the overall performance of the algorithm. In the context of the TFI model, the choice of Z as the first control Hamiltonian tends to be more effective than opting for X .

We also introduce additional plots that extend the analysis of the TFI model with variations in parameters. Fig. 15 provides insights into the performance of the CD-FQA across three TFI models characterized by distinct parameter sets, $h_x = -0.4, -1.4$, and 1.4 . For the case of $h_x = -0.4$, the ground state is in an antiferromagnetic phase. The performance of CD-FQA protocol is similar

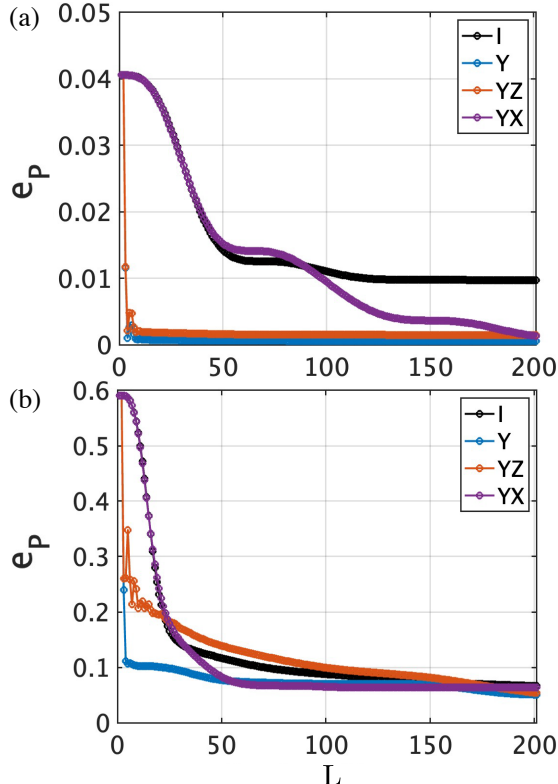


FIG. 14. The CD-FQA protocol for the TFI with alternate first control Hamiltonian $H_1 = Z$ for $h_x =$ (a) 0.4 , (b) 1.4 . The initial state is the ground state of Z .

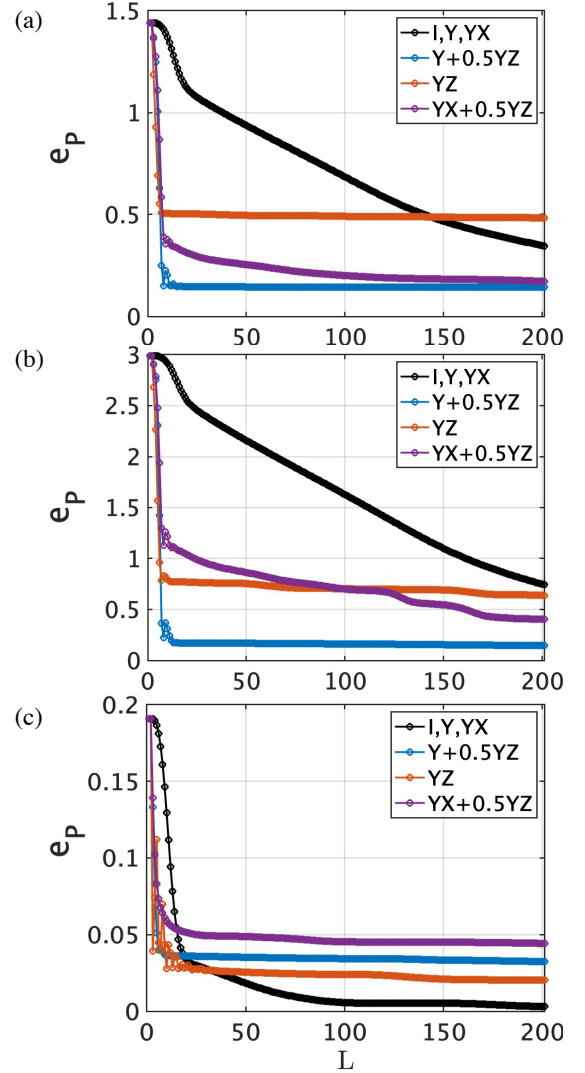


FIG. 15. The CD-FQA protocol for additional cases for the TFI with $h_x =$ (a) -0.4 , (b) -1.4 , (c) 1.4 .

to that shown in Fig. 9 in the main text. When the $|h_x| > 1$, the spins in the ground state are more likely to be aligned along x-axis. Therefore, the YX operator does not play any significant role compared to the YZ operator, see Figs. 15b,c. Finally, when $h_x > 1$, the ground state is close to the initial state and therefore we see a fast convergence using the standard FQA.

Appendix B: Simulation on PennyLane

In the main text, simulation results were presented for unitaries without Trotterization. However, in practical quantum devices, it is common practice to execute unitary (time) evolutions using the Trotter approximation. In Fig. 16, we showcase a classical simulation conducted through the application of PennyLane tools in the first-order Trotter approximation. For demonstration pur-

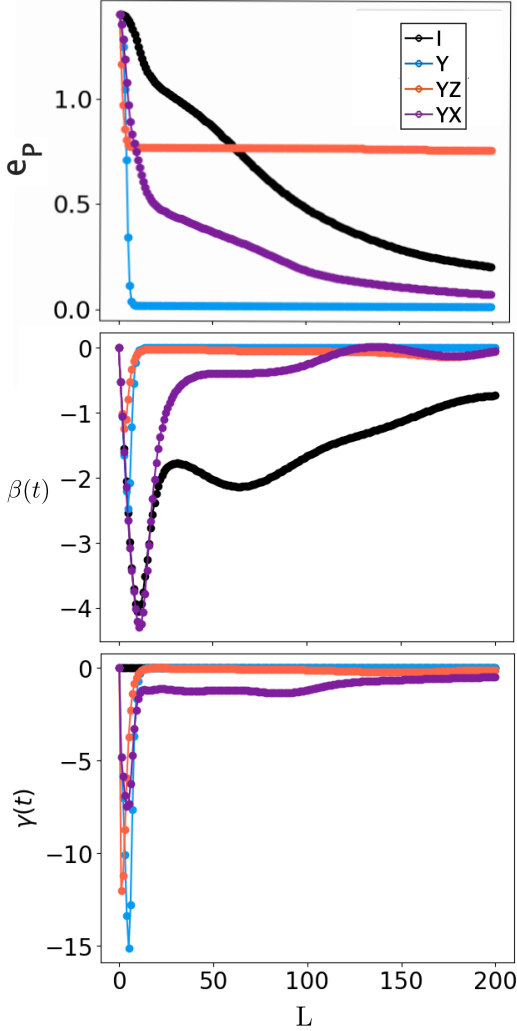


FIG. 16. FQA simulation results for LFI with $N = 6$, $\Delta t = 0.01$, $\alpha = 6$, and parameters $\{h_z, h_x\} = \{0.4, 0.0\}$. The simulation was performed with PennyLane [64], where each unitary evolution is implemented with the first-order Trotter approximation. The result is consistent with the quasi-exact simulation without Trotterization presented in Fig. 2.

poses, we choose the LFI model, and the plots affirm the consistency of the curves with the results previously depicted in Fig. 2.

Appendix C: Effects of statistical errors

The experimental results are affected by two sources of error: gate errors, and statistical errors when evaluating expectation values. We show in Fig. 17 that the dynamics does not accumulate statistical errors with circuit depth L , and thus can easily be made negligible compared to the gate errors by increasing the repetition number for

each measurement. The reason for the non-accumulation

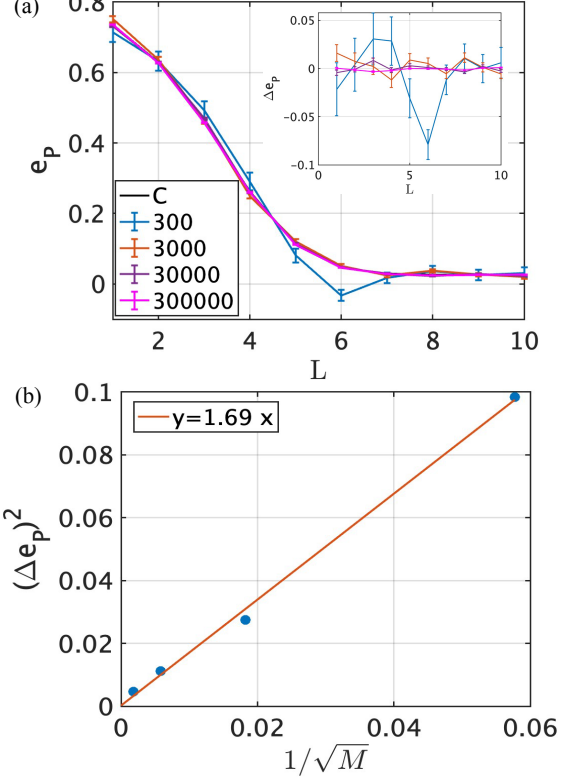


FIG. 17. (a) The average energy vs the circuit depth is plotted for CD-FQA with Y as the CD operator for different number of measurement samples, M . Here, “C” refers to the classical simulation where expectation values are calculated directly. The inset shows the deviation of energy from the classical simulation result. (b) The standard deviations for different sample sizes are shown and fitted linearly with $1/\sqrt{M}$ (red line). The standard deviation is obtained from the energy deviations across all layers.

is that, if we obtain β 's and γ 's with some uncertainties, it effectively changes the parameter α as in Eq. (12) slightly for each layer. When the uncertainties are small, we will obtain another parameter trajectory for β 's and γ 's close to the exact ones, typically leading to the same converged energies. Thus the statistical error will not accumulate during the feedback-based protocol. The overall uncertainty due to statistical errors is proportional to $\frac{1}{\sqrt{M}}$, where M is the number of repetitions for each measurement. To showcase the argument, we did “dry-run” simulations of our protocol, where we performed repetitive measurements on a noiseless classical simulator for quantum circuits to get expectation values, compared to the results obtained from directly calculating the expectation values of states. The results in Fig. 17(b) demonstrate that the statistical errors do not accumulate and converge to the same energy values.

-
- [1] D. Poulin and P. Wocjan, *Phys. Rev. Lett.* **102**, 130503 (2009).
- [2] N. M. Tubman, C. Mejuto-Zaera, J. M. Epstein, D. Hait, D. S. Levine, W. Huggins, Z. Jiang, J. R. McClean, R. Babbush, M. Head-Gordon, and K. B. Whaley, (2018), arXiv:1809.05523 [quant-ph].
- [3] Y. Ge, J. Tura, and J. I. Cirac, *Journal of Mathematical Physics* **60**, 022202 (2019).
- [4] L. Lin and Y. Tong, *Quantum* **4**, 372 (2020).
- [5] Y. Wang, C. Zhu, M. Jing, and X. Wang, (2023), arXiv:2303.11204 [quant-ph].
- [6] E. Farhi, J. Goldstone, S. Gutmann, and M. Sipser, (2000), arXiv:quant-ph/0001106 [quant-ph].
- [7] A. Aspuru-Guzik, A. D. Dutoi, P. J. Love, and M. Head-Gordon, *Science* **309**, 1704 (2005).
- [8] E. Farhi, J. Goldstone, S. Gutmann, J. Lapan, A. Lundgren, and D. Preda, *Science* **292**, 472 (2001).
- [9] T. Albash and D. A. Lidar, *Rev. Mod. Phys.* **90**, 015002 (2018).
- [10] A. Finnila, M. Gomez, C. Sebenik, C. Stenson, and J. Doll, *Chemical Physics Letters* **219**, 343 (1994).
- [11] T. Kadowaki and H. Nishimori, *Phys. Rev. E* **58**, 5355 (1998).
- [12] J. Brooke, D. Bitko, T. F., null, and G. Aeppli, *Science* **284**, 779 (1999).
- [13] J. Preskill, *Quantum* **2**, 79 (2018).
- [14] J. R. McClean, J. Romero, R. Babbush, and A. Aspuru-Guzik, *New Journal of Physics* **18**, 023023 (2016).
- [15] C. Bravo-Prieto, R. LaRose, M. Cerezo, Y. Subasi, L. Cincio, and P. J. Coles, *Quantum* **7**, 1188 (2023).
- [16] H. R. Grimsley, S. E. Economou, E. Barnes, and N. J. Mayhall, *Nature Communications* **10**, 3007 (2019).
- [17] M. Cerezo, A. Arrasmith, R. Babbush, S. C. Benjamin, S. Endo, K. Fujii, J. R. McClean, K. Mitarai, X. Yuan, L. Cincio, and P. J. Coles, *Nature Reviews Physics* **3**, 625 (2021).
- [18] A. B. Magann, C. Arenz, M. D. Grace, T.-S. Ho, R. L. Kosut, J. R. McClean, H. A. Rabitz, and M. Sarovar, *PRX Quantum* **2**, 010101 (2021).
- [19] K. Bharti, A. Cervera-Lierta, T. H. Kyaw, T. Haug, S. Alperin-Lea, A. Anand, M. Degroote, H. Heimonen, J. S. Kottmann, T. Menke, W.-K. Mok, S. Sim, L.-C. Kwek, and A. Aspuru-Guzik, *Rev. Mod. Phys.* **94**, 015004 (2022).
- [20] E. Farhi, J. Goldstone, and S. Gutmann, (2014), arXiv:1411.4028 [quant-ph].
- [21] S. Lloyd, “Quantum approximate optimization is computationally universal,” (2018), arXiv:1812.11075 [quant-ph].
- [22] A. M. Dalzell, A. W. Harrow, D. E. Koh, and R. L. La Placa, *Quantum* **4**, 264 (2020).
- [23] A. Peruzzo, J. McClean, P. Shadbolt, M.-H. Yung, X.-Q. Zhou, P. J. Love, A. Aspuru-Guzik, and J. L. O’Brien, *Nature Communications* **5**, 4213 (2014).
- [24] A. Kandala, A. Mezzacapo, K. Temme, M. Takita, M. Brink, J. M. Chow, and J. M. Gambetta, *Nature* **549**, 242 (2017).
- [25] J. I. Colless, V. V. Ramasesh, D. Dahmen, M. S. Blok, M. E. Kimchi-Schwartz, J. R. McClean, J. Carter, W. A. de Jong, and I. Siddiqi, *Phys. Rev. X* **8**, 011021 (2018).
- [26] J. Tilly, H. Chen, S. Cao, D. Picozzi, K. Setia, Y. Li, E. Grant, L. Wossnig, I. Runger, G. H. Booth, and J. Tennyson, *Physics Reports* **986**, 1 (2022).
- [27] L. Zhou, S.-T. Wang, S. Choi, H. Pichler, and M. D. Lukin, *Phys. Rev. X* **10**, 021067 (2020).
- [28] X. Liu, A. Angone, R. Shaydulin, I. Safro, Y. Alexeev, and L. Cincio, *IEEE Transactions on Quantum Engineering* **3**, 1 (2022).
- [29] Y. Cao, J. Romero, J. P. Olson, M. Degroote, P. D. Johnson, M. Kieferová, I. D. Kivlichan, T. Menke, B. Peropadre, N. P. D. Sawaya, S. Sim, L. Veis, and A. Aspuru-Guzik, *Chemical Reviews* **119**, 10856 (2019).
- [30] R. Chakrabarti and H. Rabitz, *International Reviews in Physical Chemistry* **26**, 671 (2007).
- [31] B. Russell, H. Rabitz, and R.-B. Wu, *Journal of Physics A: Mathematical and Theoretical* **50**, 205302 (2017).
- [32] J. R. McClean, S. Boixo, V. N. Smelyanskiy, R. Babbush, and H. Neven, *Nature Communications* **9**, 4812 (2018).
- [33] R. Wiersema, C. Zhou, Y. de Sereville, J. F. Carrasquilla, Y. B. Kim, and H. Yuen, *PRX Quantum* **1**, 020319 (2020).
- [34] L. Bittel and M. Kliesch, *Phys. Rev. Lett.* **127**, 120502 (2021).
- [35] M. Larocca, P. Czarnik, K. Sharma, G. Muraleedharan, P. J. Coles, and M. Cerezo, *Quantum* **6**, 824 (2022).
- [36] A. B. Magann, K. M. Rudinger, M. D. Grace, and M. Sarovar, *Phys. Rev. Lett.* **129**, 250502 (2022).
- [37] A. B. Magann, K. M. Rudinger, M. D. Grace, and M. Sarovar, *Phys. Rev. A* **106**, 062414 (2022).
- [38] S. Grivopoulos and B. Bamieh, in *42nd IEEE International Conference on Decision and Control (IEEE Cat. No.03CH37475)*, Vol. 1 (2003) pp. 434–438 Vol.1.
- [39] L. C. Wang, M. Jiang, C. Chen, D. Dong, S. Cong, and F. Meng, *The Scientific World Journal* **2013**, 967529 (2013).
- [40] M. Demirplak and S. A. Rice, *The Journal of Physical Chemistry A* **107**, 9937 (2003).
- [41] J. Yao, L. Lin, and M. Bukov, *Phys. Rev. X* **11**, 031070 (2021).
- [42] P. Chandarana, N. N. Hegade, K. Paul, F. Albarrán-Arriagada, E. Solano, A. del Campo, and X. Chen, *Phys. Rev. Res.* **4**, 013141 (2022).
- [43] C. M. Keever and M. Lubasch, “Towards adiabatic quantum computing using compressed quantum circuits,” (2023), arXiv:2311.05544 [quant-ph].
- [44] K. Beauchard, J. M. Coron, M. Mirrahimi, and P. Rouchon, *Systems and Control Letters* **56**, 388 (2007).
- [45] S. Zhao, H. Lin, J. Sun, and Z. Xue, *International Journal of Robust and Nonlinear Control* **22**, 1212 (2012).
- [46] J. P. La Salle, *The Stability of Dynamical Systems* (Society for Industrial and Applied Mathematics, 1976).
- [47] D. Sels and A. Polkovnikov, *Proceedings of the National Academy of Sciences* **114**, E3909 (2017).
- [48] X. Chen, A. Ruschhaupt, S. Schmidt, A. del Campo, D. Guéry-Odelin, and J. G. Muga, *Phys. Rev. Lett.* **104**, 063002 (2010).
- [49] A. del Campo, *Phys. Rev. Lett.* **111**, 100502 (2013).
- [50] D. Guéry-Odelin, A. Ruschhaupt, A. Kiely, E. Torrontegui, S. Martínez-Garaot, and J. G. Muga, *Rev. Mod. Phys.* **91**, 045001 (2019).

- [51] K. Takahashi, *Journal of the Physical Society of Japan* **88**, 061002 (2019).
- [52] P. W. Claeys, M. Pandey, D. Sels, and A. Polkovnikov, *Phys. Rev. Lett.* **123**, 090602 (2019).
- [53] I. Čepaitė, A. Polkovnikov, A. J. Daley, and C. W. Duncan, *PRX Quantum* **4**, 010312 (2023).
- [54] P. Gokhale, O. Angiuli, Y. Ding, K. Gui, T. Tomesh, M. Suchara, M. Martonosi, and F. T. Chong, (2019), arXiv:1907.13623 [quant-ph].
- [55] V. Verteletskyi, T.-C. Yen, and A. F. Izmaylov, *The Journal of Chemical Physics* **152**, 124114 (2020).
- [56] B. Reggio, N. Butt, A. Lytle, and P. Draper, (2023), arXiv:2305.11847 [quant-ph].
- [57] P. G. Anastasiou, N. J. Mayhall, E. Barnes, and S. E. Economou, (2023), arXiv:2306.03227 [quant-ph].
- [58] L. Zhu, S. Liang, C. Yang, and X. Li, (2023), arXiv:2307.06504 [quant-ph].
- [59] N. N. Hegade, X. Chen, and E. Solano, *Phys. Rev. Res.* **4**, L042030 (2022).
- [60] S. Bravyi, M. B. Hastings, and F. Verstraete, *Phys. Rev. Lett.* **97**, 050401 (2006).
- [61] N. Yu and T.-C. Wei, (2023), arXiv:2303.08938 [quant-ph].
- [62] K. Temme, S. Bravyi, and J. M. Gambetta, *Physical review letters* **119**, 180509 (2017).
- [63] T. Giurgica-Tiron, Y. Hindy, R. LaRose, A. Mari, and W. J. Zeng, in *2020 IEEE International Conference on Quantum Computing and Engineering (QCE)* (IEEE, 2020) pp. 306–316.
- [64] V. Bergholm, J. Izaac, M. Schuld, C. Gogolin, S. Ahmed, V. Ajith, M. S. Alam, G. Alonso-Linaje, B. Akash-Narayanan, A. Asadi, J. M. Arrazola, U. Azad, S. Banning, C. Blank, T. R. Bromley, B. A. Cordier, J. Ceroni, A. Delgado, O. D. Matteo, A. Dusko, T. Garg, D. Guala, A. Hayes, R. Hill, A. Ijaz, T. Isacsson, D. Ittah, S. Jhangiri, P. Jain, E. Jiang, A. Khandelwal, K. Kottmann, R. A. Lang, C. Lee, T. Loke, A. Lowe, K. McKiernan, J. J. Meyer, J. A. Montañez-Barrera, R. Moyard, Z. Niu, L. J. O’Riordan, S. Oud, A. Panigrahi, C.-Y. Park, D. Polatajko, N. Quesada, C. Roberts, N. Sá, I. Schoch, B. Shi, S. Shu, S. Sim, A. Singh, I. Strandberg, J. Soni, A. Száva, S. Thabet, R. A. Vargas-Hernández, T. Vincent, N. Vitucci, M. Weber, D. Wierichs, R. Wiersema, M. Willmann, V. Wong, S. Zhang, and N. Killoran, (2022), arXiv:1811.04968 [quant-ph].